Bulletin of the Seismological Society of America, Vol. 86, No. 1B, pp. S156–S167, February 1996

Modeling of Ground Motion from a 1994 Northridge Aftershock Using a Tomographic Velocity Model of the Los Angeles Basin

by Jennifer S. Haase, Egill Hauksson, Frank Vernon, and Adam Edelman

Abstract The 1994 Northridge mainshock and its aftershocks show a complex pattern of peak accelerations at stations located in the Los Angeles Basin. The waveforms contain multiples of body-wave phases and extensive surface waves at frequencies mostly below 1 Hz. In particular, for stations at distances greater than 18 km, secondary arrivals show larger accelerations than the direct *S*-wave arrivals. The mainshock waveforms are further complicated by irregularities of the source rupture. We use 2D finite difference to evaluate the effect of lateral variations in seismic velocity on the amplitude of shear-wave energy and to distinguish the effects of source and propagation path. We model waveforms from one aftershock recorded at nine stations deployed along a 60-km-long profile extending into the Los Angeles Basin. We use a two-dimensional slice through the 3D tomography model of the Los Angeles Basin in the 2D finite-difference calculations. These synthetic waveforms fit the aftershock waveforms significantly better than corresponding waveforms determined from simple 1D velocity models. With the addition of a thin low-velocity surface layer above the tomography model, the finite-difference synthetics reproduce most of the important features of the recorded data, in particular, the large-amplitude arrivals 7 to 10 sec following the direct *S* arrival. These arrivals correspond to the *SS* arrival, which is sharply refracted at the basin edge, and the *S*-wave with multiple legs trapped by the dipping near surface gradient. For large earthquakes located either inside or outside the basin, these phases can be the cause of the largest and hence potentially most hazardous shaking in the Los Angeles Basin.

Introduction

At many sites in the Los Angeles Basin, strong-motion recordings of the 1994 M_w 6.7 Northridge earthquake show large horizontal peak accelerations in phases following the direct *S* phase. In some cases, these later phases are larger than the direct *S* wave and significantly extend the time duration of strong ground shaking. In the near-source region, some later phases were modeled using a complicated rupture source of 7-sec duration (Wald and Heaton, 1994); however, in the Los Angeles Basin, these large later phases are likely to be some combination of source and propagation effects. In particular, following the direct *S*-wave arrival by 5 sec, a horizontal peak acceleration of 0.9 *g* was measured at Santa Monica (Fig. 1; Shakal *et al.*, 1994). At several other sites, peak accelerations greater than 0.4 *g* were measured within the Los Angeles Basin in phases that followed the direct *S* wave by more than 5 sec. These sites are located at greater distances from the source than sites within the Santa Monica Mountains that recorded smaller accelerations.

Similar observations were reported from the pattern of ground motion produced by the 1971 San Fernando earthquake. The San Fernando earthquake was similar in its tectonic characteristics and location relative to the Los Angeles Basin, though it ruptured on a north-dipping fault plane (Whitcomb *et al.*, 1973; Langston, 1978; Heaton, 1982). In contrast, the Northridge earthquake ruptured on a south-dipping fault plane (Hauksson *et al.*, 1995; Wald and Heaton, 1994). Vidale and Helmberger (1988) used a 2D profile through a laterally varying basin structure to model waveforms from the San Fernando earthquake with 2D elastic finite difference. Their basin structure was derived primarily from well logs (Duke *et al.*, 1971). They reproduced the extended durations of strong motion recorded across the Los Angeles Basin that were observed in the San Fernando earthquake.

We use a similar approach here to model the ground motions from an M_L 4.3 Northridge aftershock by taking 2D slices through a 3D tomographic velocity model. The relatively simple source allows us to isolate the propagation effects from source effects. Shallow velocity structure local to the recording station has a strong influence on the recorded ground motion, especially at high frequencies. Such localized velocity anomalies are in most cases beyond the reso-

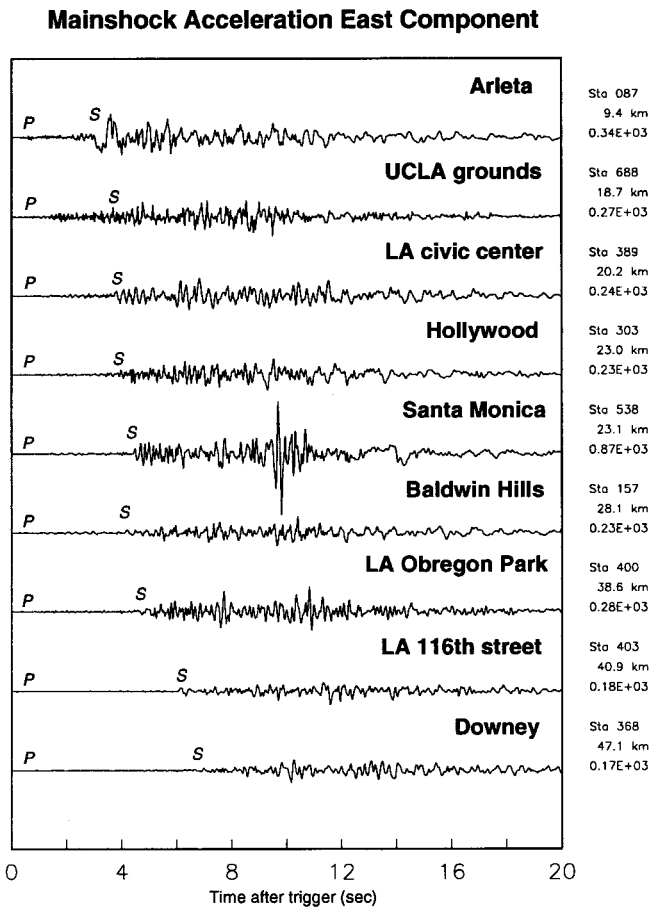

Figure 1. CSMIP strong ground motion recordings of the 17 January 1994 Northridge earthquake recorded at sites within the Los Angeles Basin. The peak horizontal acceleration for most of these records occurred more than 5 sec after the direct *S*-wave arrival. Portable weak-motion recorders were deployed near some of these sites following the mainshock. Epicentral distance and amplitude of acceleration in cm/sec^2 are given at right.

lution of the tomographic modeling. Tomography reliably images the depth to the basement and the location of the basin edge at depth. It is our primary objective to examine the extent to which this larger-scale structure affects longer-period energy in the recorded ground motions.

To evaluate the effects of shallow structure and compare them with the results from the tomographic modeling, we calculate synthetic waveforms for a standard 1D model and a 1D model with a thin low-velocity layer in the near surface (Table 1). The standard 1D SoCal model (Dreger and Helmberger, 1990) is used routinely in regional waveform inversions for source mechanisms using broadband data. The WHN model was used to model near-source (<25 km) strong-motion records from the Northridge mainshock (Wald and Heaton, 1994). It was taken from model C of Langston (1978), with the addition of a slower 0.5-km-thick layer with *P*-wave velocity of 1.0 km/sec at the surface to

Table 1
1D Velocity Models

SoCaL Model				WHN Model			
Depth (km)	*P* Vel (km/sec)	*S* Vel (km/sec)	Density (g/cm^3)	Depth (km)	*P* Vel (km/sec)	*S* Vel (km/sec)	Density (g/cm^3)
5.5	5.5	3.18	2.40	0.5	1.9	1.0	2.1
16.0	6.3	3.64	2.67	2.0	4.0	2.0	2.6
35.0	6.7	3.87	2.80	4.5	5.5	3.2	2.7
45.0	7.8	4.50	3.00	27.5	6.3	3.6	2.8
				32.5	6.8	3.9	2.9
				40.5	7.8	4.5	3.1

approximate the local Northridge structure. This model is not appropriate for the transitional structure into the greater Los Angeles Basin region, but it is well suited for modeling near stations on the receiver profile. It also demonstrates some of the effects of shallow structure at large ranges where it contributes to the generation of low-frequency coda waves.

Our approach of using 2D slices through a 3D velocity model is computationally efficient relative to a full 3D wave propagation simulation and provides a realistic way of determining gross path effects when modeling strong ground motion records. Examples of 3D wave propagation simulations in the San Bernardino Valley (Frankel, 1993) show that three-dimensional structure cannot be neglected when calculating ground motion, especially for paths that cross at a shallow angle to the dominant structural gradients. However, before attempting to model much later phases and the coda, which are much more likely to have been caused by 3D multipathing, we take advantage of the quicker 2D calculations to adjust the model to match the early body-wave phases of the waveform to first order. The computation time required for 3D calculations limits the size of regions that can be modeled at frequencies of interest for seismic hazard. Three-dimensional synthetics have been calculated for frequencies up to 0.4 Hz in the relatively large Los Angeles Basin (Day *et al.*, 1994), but higher-frequency calculations up to 1 Hz have typically been limited to model areas smaller than a 30-km range (Frankel, 1993) or a 9-km depth (Olsen and Schuster, 1995). Computer memory limits the range of velocities that can be included in the model so that 3D calculations are much more difficult when there are extremely low near-surface velocities, such as is the case in the Los Angeles Basin. Despite the presence of significant 3D propagation effects, this preliminary 2D slice modeling provides valuable insight into determining the causative structures that produce extended durations of shaking.

Improving the 3D velocity model so that it satisfies the Northridge aftershock data has more far-reaching applications than specifically modeling the Northridge aftershock. It is a step toward the ultimate goal of creating an accurate 3D model for 3D wave propagation calculations. An accurate 3D velocity model will be useful for predicting the ground motion from earthquake scenarios from other source regions, possibly using 3D finite-difference methods. In ad-

dition, it focuses efforts to improve the resolution of the 3D tomographic velocity modeling where it has the most benefit for strong ground motion modeling.

Experiment and Dataset

In the two days following the Northridge mainshock, we deployed portable instruments in cooperation with the members of the Southern California Earthquake Center (SCEC) and the USGS (Steidl *et al.,* 1994). The complete SCEC and USGS deployments included over 70 sites, but only the sites relevant to this study are shown in Figure 2. Several of these portable instruments were deployed at existing sites of the California Strong Motion Instrumentation Program (CSMIP), University of Southern California (USC), and USGS strong-motion networks. Eight of the portable stations were broadband Streckeisen STS2 instruments, and the others were strong- and weak-motion pairs of force-balanced accelerometers (FBA's) and Mark Products (L4 or L22).

In this study, we use data from nine instruments that form a linear profile extending from the epicenter of the Northridge mainshock to the south-southeast (Scott *et al.*, 1994). This profile, which includes the TERRAscope station USC, is 60-km long and provides ray paths crossing the Santa Monica Mountains into the deepest part of the Los Angeles Basin. During the two-week deployment of instruments along this profile, over 20 Northridge aftershocks were recorded with magnitudes between 3.2 and 5.0. These events are large enough to be well recorded in the noisy urban environment and small enough to have relatively simple sources. The broadband stations recorded excellent waveforms with significant low-frequency energy resonating at the basin sites for more than 10 minutes for the largest events. The FBA's recorded fine digital recordings, but low-frequency noise interferes with accurate integration of the records to displacement.

We study in detail a magnitude 4.3 event that occurred on 21 January 1994, 18:52 (UT), because preliminary evaluation of its primary body waves suggest a simple source. The record section for this event as recorded by the Los Angeles Basin profile is shown in Figure 3. The instrument response has been removed, and the velocity traces have been filtered between 0.04 and 5 Hz.

Aftershock Source Parameters

Our approach in this forward-modeling experiment is to find the best point source earthquake mechanism for this aftershock. Then we use this focal mechanism in the waveform modeling to qualitatively evaluate the effects of the basin structure on the waveforms recorded within the basin. We use two independent datasets and methods to determine a robust mechanism: first motions and regional broadband waveform inversion at distances of 100 to 150 km.

We relocated the aftershock and determined the first-motion focal mechanism using data from the Southern California Seismic Network (SCSN). We used a 1D layered velocity model and a corresponding set of station corrections specific to the Northridge area (Hauksson *et al.,* 1995). The event has origin time 18:52:43.98, latitude 34.3008°, longitude −118.4560°, depth 8.9 km, strike 100°, dip 40°, and rake 60° (Fig. 2). Including the first motions from the SCEC, portable instruments (the timing was not reliable on some instruments) changed the mechanism slightly to strike 110°, dip 35°, and rake 70°. For this focal mechanism, the first *P*-motion polarity changes from compressional to dilatational along the record section at approximately the station NHFS at a 13-km distance.

To verify the first-motion focal mechanism and to confirm that the mechanism predicts the direct *P*, *S*, and surface waves for the long-period waveforms, we modeled the regional TERRAscope records for this event. We used a grid-search inversion method (Zhao and Helmberger, 1994) to search over a range of strike, dip, rake, and depth to determine the mechanism, assuming a 0.5 0.5-sec triangle source time function. The inversion uses synthetic Green's func-

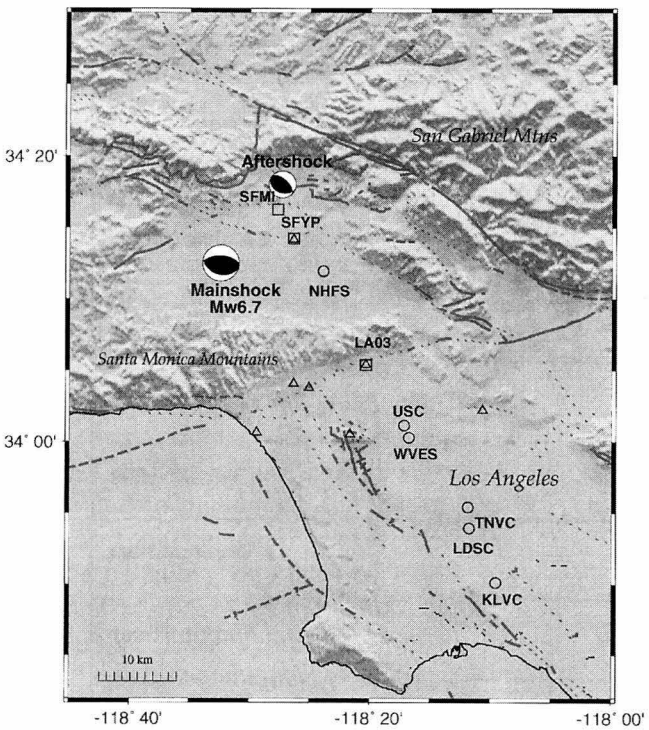

Figure 2. Map of the greater Los Angeles region showing the locations of SCEC and USGS portable instruments deployed after the Northridge earthquake in a profile crossing the basin. Four broadband STS2's were deployed in the deepest part of the Los Angeles Basin. The lower hemisphere focal mechanism of the mainshock and aftershock 94-021-18:52 are shown. Circles show STS2 sensors, squares show FBA sensors deployed after the mainshock, and triangles show the strong-motion stations that recorded the mainshock waveforms in Figure 1.

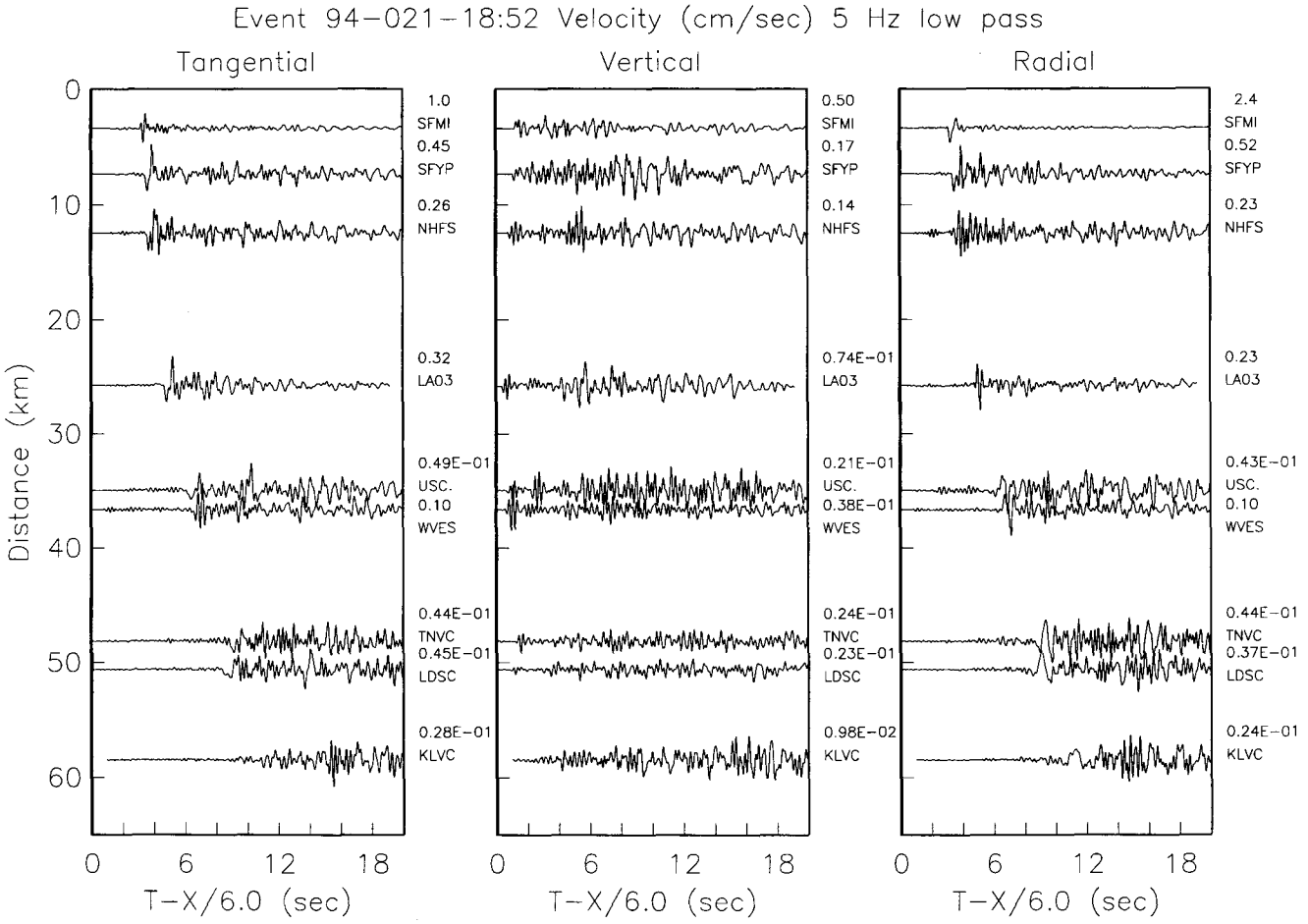

Figure 3. Velocity record section through the Los Angeles Basin for the aftershock 94-021-18:52: (a) tangential component, (b) vertical component, and (c) radial component. Amplitudes in cm/sec are shown at right. The traces are plotted with a reducing velocity of 6.0 km/sec and were filtered between 0.04 and 5 Hz.

tions computed for the 1D (southern California) SoCal model (Dreger and Helmberger, 1990; Table 1). We first modeled the data filtered with a Press-Ewing 3090 long-period response and found a mechanism very close to the first-motion solution with strike 115°, dip 30°, rake 60°, and moment equal to 2.4×10^{22} dyne-cm. We then modeled the broadband data low pass filtered at 1 Hz and found a very similar mechanism with strike 110°, dip 35°, rake 55°, and moment equal to 2.7×10^{22} dyne-cm. The waveforms from the broadband data and synthetics are shown in Figure 4. The best-fitting mechanism had a source depth of 11 km, different from the first arrival location of 8.9 km. However, the source inversion mechanism was stable for a large depth range including 8 km, and the misfit was only slightly worse. The waveform fit is in general very good for stations at regional distances and for close stations located outside of the basin, such as PAS and RPV. The surface waves on the vertical and radial components and the radial Pnl waveforms match the synthetics. The vertical Pnl waveforms at DGR, GSC, and SVD and the tangential records at stations DGR, GSC, PAS, and SVD do not match as well. USC, which is in the center of the Los Angeles Basin, could not be modeled with these simple 1D Green's functions, so it was excluded from the inversion. The same problem occurred when we attempted to include data from the broadband portable stations in the inversion for mechanism. The simple 1D Green's functions were not close enough to the real Green's functions that the data could contribute to resolving the solution. This is what we expected for these stations and what we ultimately want to correct with a laterally varying velocity structure.

Having confirmed the mechanism using the TERRAscope data, we proceed with the finite-difference calculations using the depth and mechanism of the first-motion solution and the moment estimated from the long-period data.

Three-Dimensional Velocity Model

A three-dimensional *P*-wave velocity model of the Los Angeles Basin region has been determined from arrival-time

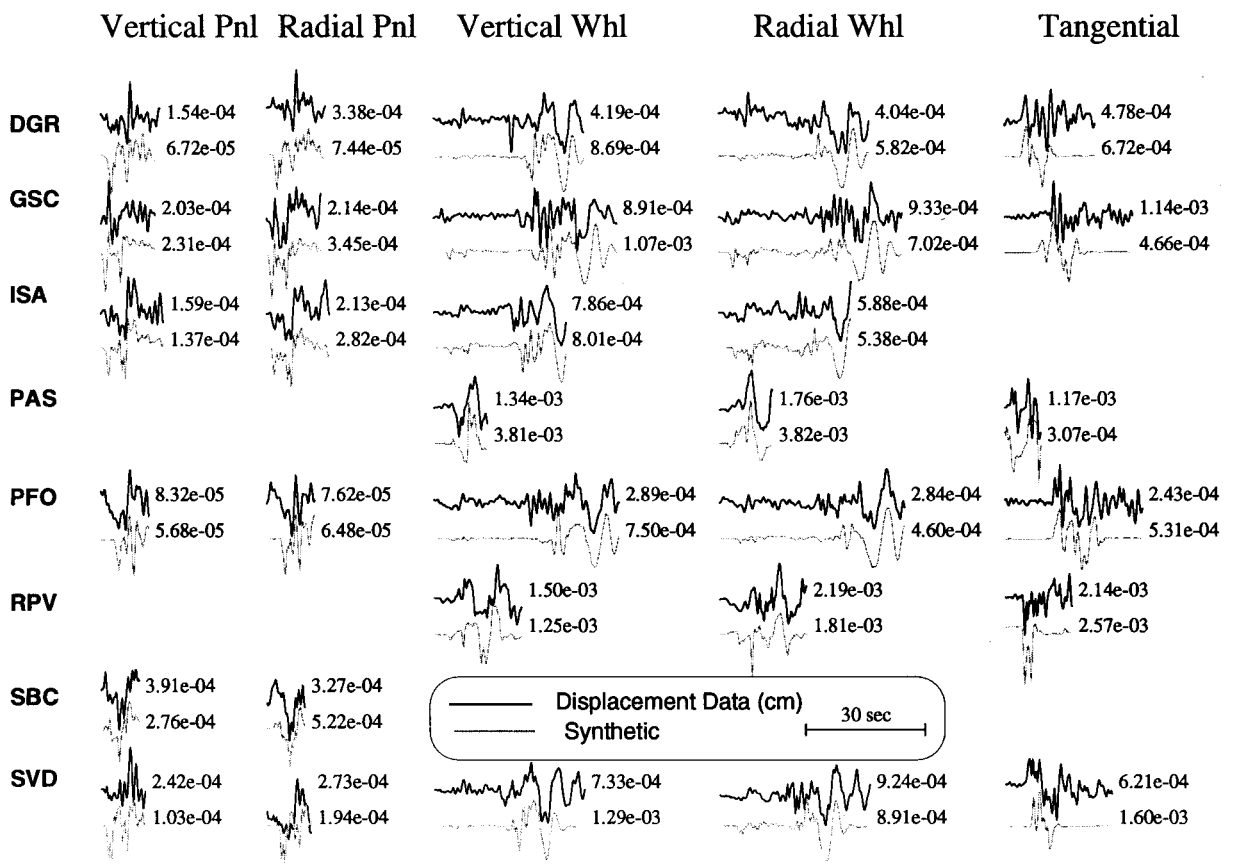

Figure 4. Waveform fits for TERRAscope stations used in the broadband waveform source inversion. All stations except PAS and RPV are at greater than 110-km distance. The velocity data have been low pass filtered at 1 Hz and integrated to displacement. Amplitudes are shown in cm. The solid lines show the data, and the dashed lines show the synthetics.

data from the Southern California Seismic Network (SCSN) and the USC Seismic Network (Hauksson and Scott, 1994). We have extended this modeling to include the 3D variation of the *Vp/Vs* ratio using the *S*-wave arrival times (Hauksson and Haase, in preparation). The simultaneous inversion for earthquake hypocenters, 3D *P*-wave velocity, and 3D *Vp/Vs* ratio was done using the method of Thurber (1993) and Eberhart-Phillips (1993). This 3D model provides a good starting point for more detailed modeling of the aftershock waveforms because it satisfies a comprehensive travel-time dataset for the region and predicts the first-arrival times accurately.

The 3D *S*-wave model (Fig. 5) closely mimics the *P*-wave model, except where the data constrain significant variation in the *Vp/Vs* ratio. At depths less than 4 km, the model shows the horizontal extent of the low-velocity sedimentary units of the Los Angeles Basin. In contrast, the southern edge of the Santa Monica Mountains and the uplifted basement on the Palos Verdes Peninsula correspond to high near-surface velocities. North-dipping features adjacent to the Santa Monica fault are clearly visible in cross sections of the *S*-wave velocity perpendicular to the northern basin edge (Fig. 6).

The southern part of the San Fernando Valley was also included in the tomography modeling. Significant velocity variation exists where the model overlaps the San Fernando Valley to indicate the existence of very slow velocities at a shallow depth beneath the valley. However, the resolution is poor at the edges of the model near the aftershock epicenter, which limits the accuracy of the waveform predictions for the closest stations.

The overall appearance of the model, with a steep vertical gradient at 3- to 5-km depth, to some extent results from the starting 1D model used for the tomography, since the resolution is not good enough to perturb shallow structure significantly. However, the lateral variation of near-surface velocity at the basin edges is well resolved because of the density of stations there.

2D Finite-Difference Results

We use 2D finite-difference calculations to determine which features of the 3D velocity model contribute the most

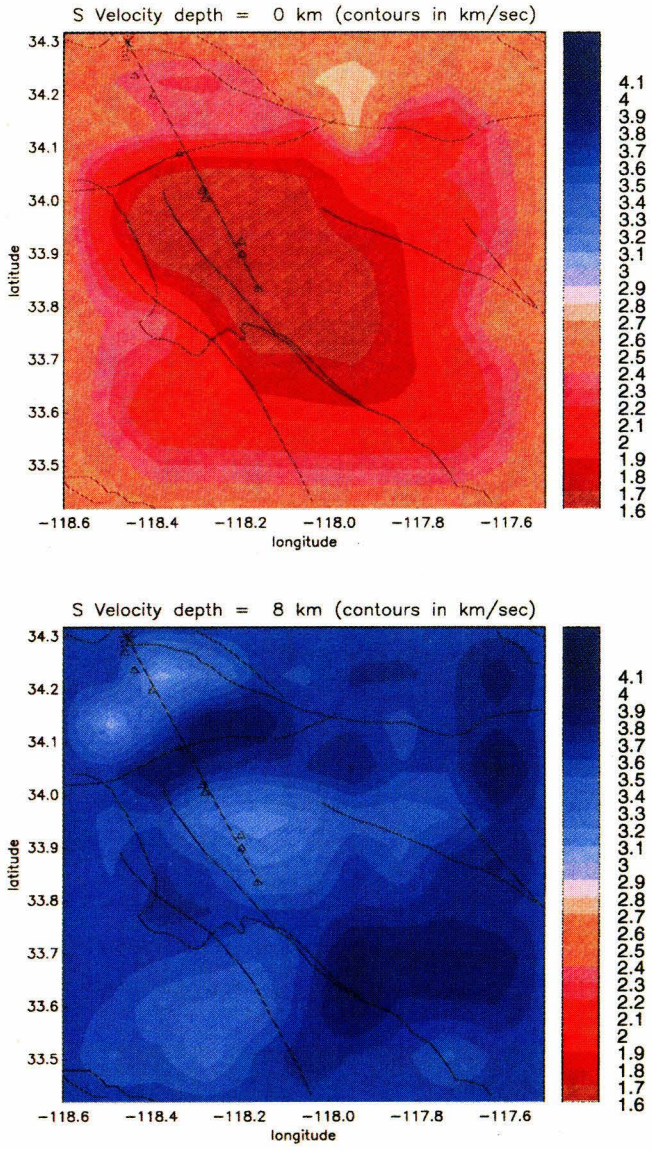

Figure 5. 3D *S*-wave velocity model (Hauksson and Scott, 1994) derived from local earthquake travel times in the Los Angeles Basin. (a) Horizontal section at 2-km depth. (b) Horizontal section at 8-km depth. Contour interval is 0.1 km/sec. The Palos Verdes fault bounds the basin region of slow velocities on the west, the Whittier fault bounds the basin on the east, and the Santa Monica fault bounds the basin on the north. Triangles indicate the stations used in this study. The solid line indicates the vertical cross section of the 3D model (Fig. 6) that was used in the finite-difference calculation.

to high-amplitude energy in the synthetic waveforms. We compare them with synthetics calculated from layered 1D velocity models. This allows us to determine the most likely origin of the high-amplitude energy found in the recorded data.

The vertical section through the tomographic velocity model (Fig. 6) was used to calculate 2D tangential finite-difference seismograms (Vidale *et al.*, 1985; Helmberger and Vidale, 1988). The cross section approximately follows the line of deployed instruments. The velocities were interpolated on a 32- by 68-km vertical grid at 100-m intervals from the tomographic *S*-wave velocity model. The density was fixed at $2.65 g/cm^3$ at all depths for these initial calculations to investigate the effects of velocity alone. A time step of 0.01 sec was used in this fourth-order scheme. The implementation of an analytic source in a 2D medium and the requirement for the transformation of the resulting linear source to a point source is discussed in Vidale *et al.* (1985). The source time function is a gaussian pulse with width approximately 0.2 sec. There is no mechanism in the algorithm for computing the attenuation, and because we are primarily interested in the effects of the 3D velocity anomalies, no attenuation correction was made.

Time slices of the amplitude of the strike-slip and dip-slip components of the tangential motion are shown at every point within the model at 3-sec intervals (Fig. 7) from depths of 0 to 12 km. The image shows that the source remains on because of the method used to calculate the wave field for a finite source-time function without the source region behaving as a rigid reflector (see Alterman and Karal, 1968). At 6 sec, the reflected *SS* wavefront appears following the direct wave. The direct wavefront has a flattened leading edge due to traveling through the region where high-velocity material rises up beneath the Santa Monica Mountains. At 9 sec, the *SS* wavefront is partially reflected upward by the steep vertical velocity gradient to form the first surface-layer multiple. At 12 sec, this first surface-layer multiple is reflected from the surface, and subsequent frames show that this energy is trapped in the basin and does not propagate below the steep horizontal gradient. At 15 to 18 sec, the *SS* wave arrives distinctly in advance of the first surface-layer multiple at ranges greater than approximately 40 km. At closer distances, these waves constructively interfere to produce large amplitudes at approximately 30- to 35-km range. The appearance of this phase and its timing are sensitive to the mid-crustal velocity gradient at the edge of the basin (Scrivner and Helmberger, 1994). At 18 to 20 sec, the second and later surface multiples are seen. The time interval between the *S*-wave and the surface-layer multiples and the amplitudes of these multiples are sensitive to the varying depth of the steep vertical velocity gradient. USC and WVES are at approximately the correct distance to see the predicted *SS* arrival as it separates from the near-surface multiple. The waveform data at USC and WVES show significant differences, though they are less than 2 km apart, which may be due to the sensitivity to this constructive interference.

The synthetic record section (Fig. 8) shows the tangential component seismograms for the source with 9-km depth and first-motion mechanism of strike 110°, dip 35°, and rake 70°. The prominent second phase is the *S* wave with a multiple leg in the near-surface low velocities. At 39 km, it starts to separate into two peaks with the *SS* phase preceding. The amplitude of this surface-layer multiple relative to the direct arrival increases with distance to a range of 50 km and is

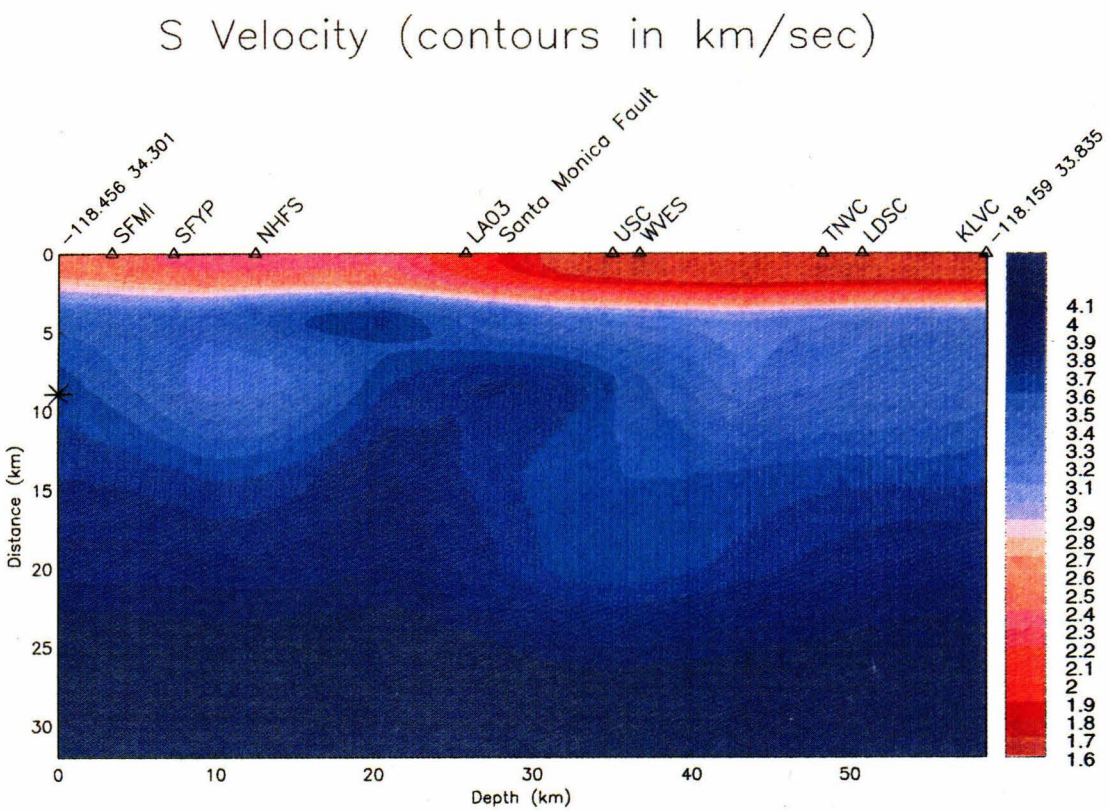

Figure 6. Cross section through the 3D velocity model (Hauksson and Scott, 1994) parallel to the line of receivers in the Los Angeles Basin. The position of the source for aftershock 94-021-18:52 is shown at 8.9-km depth on the left axis. Distance is in kilometers along the horizontal axis. Contour interval is 0.1 km/sec. The model, to first order, shows a sharp vertical gradient that varies from about 2 to 4 km in depth. There is a sharp lateral gradient at the edge of the basin at the Santa Monica fault.

larger than the direct *S* wave, an effect noticed in previous modeling using dipping constant-velocity layered structures (Helmberger and Vidale, 1988). The second surface-layer multiple appears with appreciable energy starting at about 30-km range and also increases in amplitude relative to the direct arrival as distance increases. The third and fourth multiples are also clearly seen within the range of this experiment.

The synthetic seismograms are very simple at small ranges within the San Fernando Valley, despite the basin structure present there in the 3D velocity model. The smooth model does not trap surface-wave energy like the layered model of Vidale and Helmberger (1988). Therefore, our synthetics do not produce the phenomena of surface-wave energy present in the San Fernando Valley being damped out as it passes through the Santa Monica Mountains. This would require a very high resolution tomography model of the San Fernando Valley. We can observe only the generation of surface-wave energy as it enters the Los Angeles Basin.

Comparison of Synthetics with Data

We examine in detail the tangential seismograms from stations along the Los Angeles Basin profile and compare them with synthetic waveforms predicted from the 2D finite difference (FD). We also compare them with waveforms computed from the SoCal and WHN 1D models (Table 1). The 1D synthetics were computed using wavenumber integration (Saikia, 1994). The 1D and 2D synthetics were convolved with a 0.5 0.5-sec triangle source function.

The impulsive SoCal synthetic (labeled s8) (Fig. 9) is much simpler than the recorded waveforms and can match only the first-motion polarity. The WHN model (labeled w8) is an improvement in that it produces some large surface waves directly following the *S* arrival and delays the *S* waves.

The FD synthetics (labeled f8) for the closest three stations do not show more structure than the SoCal model because of the smoothness of the model. At LA03 (the first station within the basin proper), the sharply refracted *SS* ar-

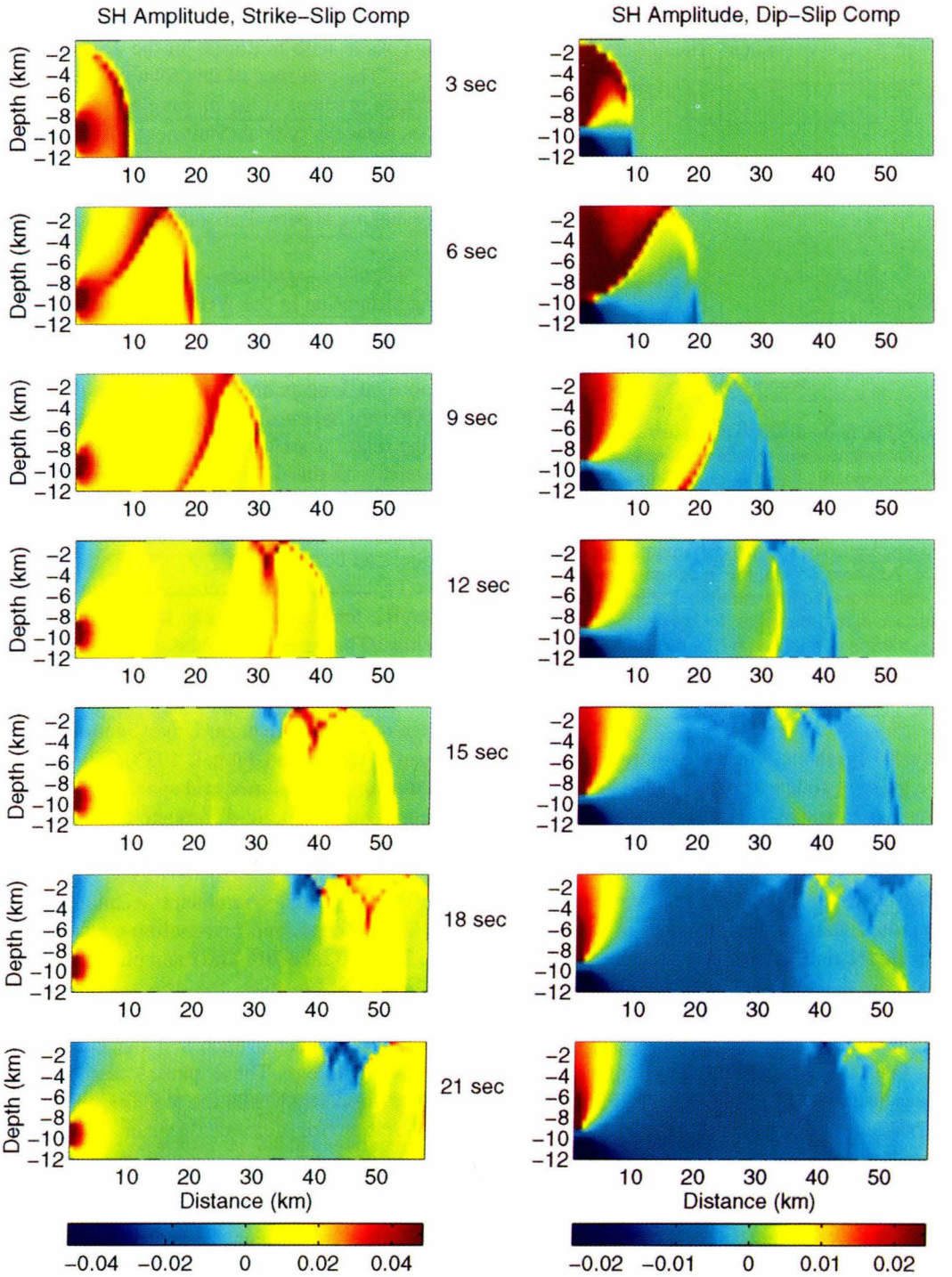

Figure 7. Time slices of the tangential wave field at 3-sec increments from the 2D finite-difference calculation for the model shown in Figure 6. (a) Strike-slip component. (b) Dip-slip component. Amplitude is given in cm of displacement. At 6 sec, the surface reflection follows the direct *S*-wave arrival, and the direct wavefront flattens as it encounters steep lateral velocity gradients. At 9 sec, the first surface multiple appears, which has reflected off the steep vertical velocity gradient. At 12 sec, the first surface multiple of the direct *S* wave is reflected from the surface and the *SS* arrival at depth advances relative to it. At 15 sec, the second surface multiple appears and the *SS* arrival occurs distinctly in advance of the first surface multiple. At 18 sec, the second surface multiple is reflected from the surface, and the first surface multiple reflection from the *SS* arrival appears. At 21 sec, the first surface multiple of the *SS* arrival is seen at about a 45- to 50-km range.

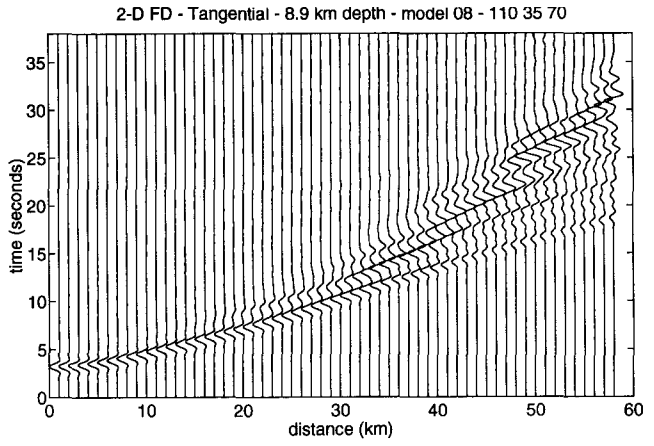

Figure 8. 2D finite-difference synthetic *SH* tangential displacement seismograms for a source at 8.9-km depth corresponding to the wave field shown in Figure 7. The mechanism is strike 110°, dip 35°, and rake 70°. The second arrival at 20 to 35 km is the *S* wave with a multiple leg above the sharp gradient near the surface. At about 38 km, the lower-amplitude *SS* wave separates from the first multiple. Later high-amplitude surface-layer multiples follow in the wave train. Each trace is normalized by the peak amplitude.

rival appears on the synthetic, but the amplitude of the following positive pulse is underestimated. Unlocked clocks at portable stations LA03 and WVES with errors on the order of 2 sec make comparisons of absolute arrival times impossible. The FD synthetics for station WVES are consistent with the first two downward pulses and the relative timing of the following two pulses, though the mismatch in relative amplitudes makes correlation of the phases ambiguous. The differences between the recorded waveforms at USC and WVES, located only 2 km apart, suggest that some of the waveform complexities are caused by variations in the velocity structure that have wavelengths smaller than 2 km or small differences in focusing of the energy. Farther along the profile at TNVC and LDSC, the synthetics match the data well with a predominantly downward motion of the first packet of arrivals followed by a packet of three upward pulses. The synthetics show the general long-period wave shape of the first 15 sec of the data, but the timing of the large negative peak is early. Comparison with the 1D WHN synthetics indicates that modifying the model to have lower near-surface velocities may help disperse these arrivals to be more consistent with the data. The amplitudes of the FD synthetics are higher than those of the data. This is probably due to our neglect of attenuation in the modeling. The 1D synthetics include the same attenuation used in the source modeling for the moment so they more accurately match the peak displacement.

Overall, the FD synthetics reproduce most of the important features of the recorded data, in particular, the larger-amplitude arrivals 7 to 10 sec after the direct *S* arrival. These arrivals correspond to the sharply refracted *SS* arrival and the *S* wave with multiples in the near-surface low-velocity layers. The presence of this *SS* wave is very sensitive to the velocity gradient at the dipping basin edge where the angle of incidence is critical (Scrivner and Helmberger, 1994). Because these phases are trapped by the dipping gradient at the basin edge, they can extend the duration of the most hazardous shaking at periods at and below 1 Hz in the Los Angeles Basin.

There is significant lower-frequency energy of even longer duration in the WHN 1D model synthetics caused by generation of surface waves in the extremely low-velocity layer. In this respect, the synthetics mimic the extended durations of long-period energy in the data. However, these waveforms when differentiated have the peak acceleration at the direct *S* arrival, not 5 to 10 sec afterward. The comparison with this 1D model illustrates the importance of including a low-velocity layer very close to the surface and indicates where a possible improvement to the 3D velocity model can be made.

To test this interpretation, we modified the 2D slice from the tomography model to have lower near-surface velocities. The velocities in the top 0.5 km of the model were reduced by 50% to preserve the lateral variations in the model and bring the surface velocities down to within the range reported from hazard investigations in the Los Angeles Basin (Tinsley and Fumal, 1985). The larger range of velocities required a finer grid spacing of 80 m to preserve the accuracy of the finite-difference calculation. The time step, density, and source-time function were the same as the initial FD calculation. Figure 10 shows the synthetic record section for the tangential component seismograms for the source with 9-km depth and first-motion mechanism of strike 110°, dip 35°, and rake 70°. The main phases are the same as those in Figure 8; however, the direct *S* arrival is later, and the time interval between phases is longer, particularly between the phases reflected once and twice above the steep near-surface gradient. These phases also have a significantly larger pulse width, and the low-frequency coda is extended in duration for distances greater than about 25 km. The finite-difference synthetics with the thin low-velocity layer (labeled f81) are also compared with the data in Figure 9. For the near-source stations, the direct *S* wave has a secondary pulse, as does the WHN model. At station LA03, the surface layer produces additional complexity after the *SS* phase, as in the data, but does not make a significant improvement in fit. The waveforms at USC and WVES match much better the timing and amplitude of the two pulses of the first and second multiples above the steep near-surface gradient. At stations TNVC, LDSC, and KLVC, the timing and amplitude of the large negative peak associated with the third and fourth multiples are reproduced very well. The addition of the surface layer was successful in delaying these arrivals and increasing the low-frequency energy in the phases to bring the finite-difference seismograms into closer agreement with the observed data.

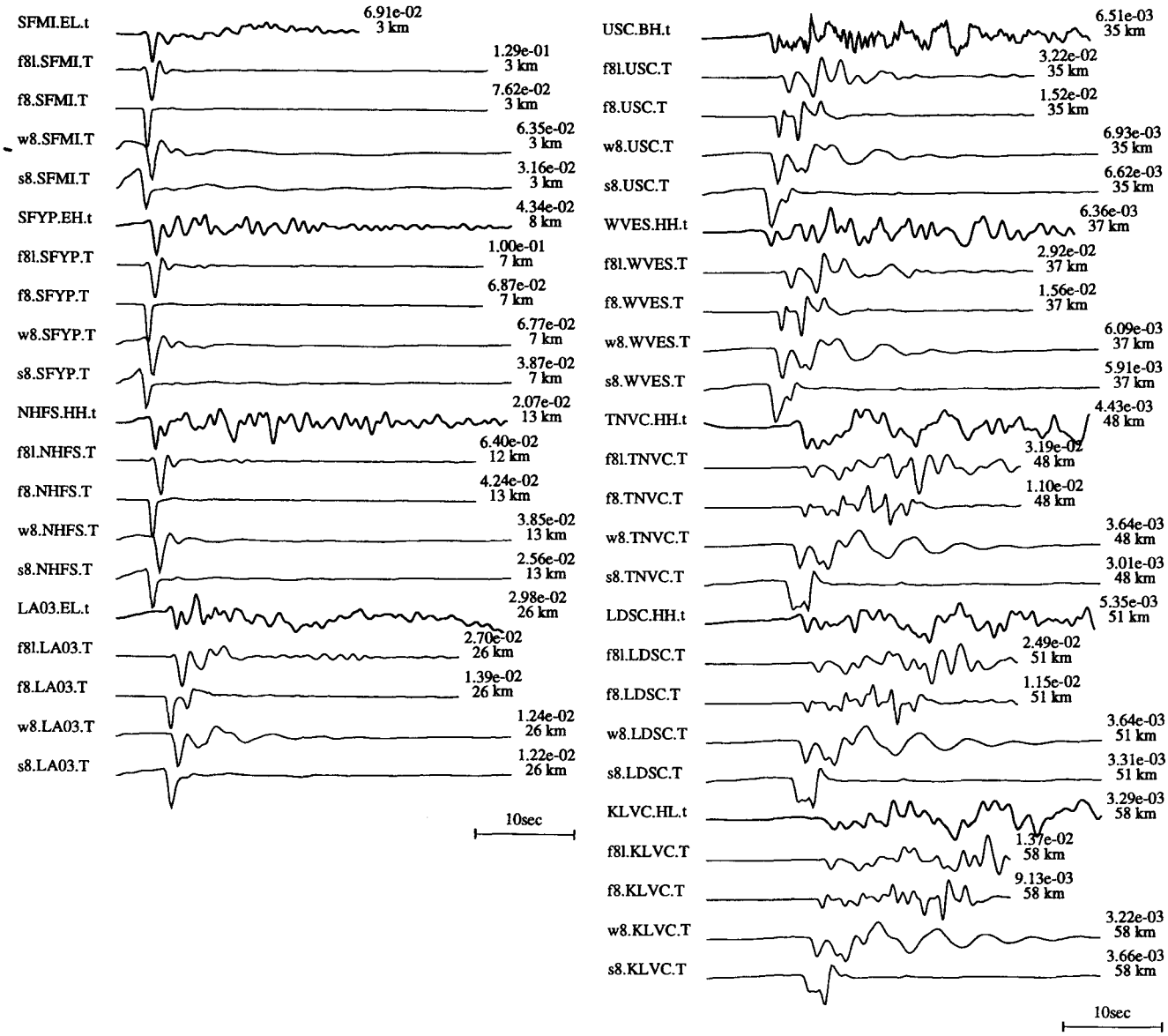

Figure 9. Comparison of tangential displacement synthetics and data for the Los Angeles Basin profile. Beneath the data at each station (heavy solid line) the synthetics are shown for the 2D finite-difference synthetics computed for the tomography model with a 0.5-km-thick low-velocity layer (labeled f81), 2D finite-difference synthetics computed for the original 3D tomography model (labeled f8), F-K synthetics from the 1D WHN model for the Northridge area (Wald and Heaton, 1994) (labeled w8), and F-K synthetics from the 1D SoCal model (Dreger and Helmberger, 1990) (labeled s8). The displacement data and synthetics are low pass filtered at 1 Hz. The amplitudes in cm are shown at the right, as well as the epicentral distance.

Discussion

When comparing the cross section of the tomographic model to other cross sections across the Los Angeles Basin that have been used for waveform modeling (Vidale and Helmberger, 1988; Scrivner and Helmberger, 1994) the striking difference is the presence of much lower near-surface shear velocities in the basin in those models, compared with the tomographic model. This is because a layer less than 1-km thick of material with very low velocities is impossible to resolve using local earthquake tomography without some other kind of constraints, such as borehole velocity measurements explicitly applied in the inversion. This leads to the question of how the tomography model with such high velocities in the basin can possibly be useful in estimating strong ground motion. The answer must lie in the consistencies among the models, which all show a 40% to 60% decrease in velocity across a lateral dimension of less than 5

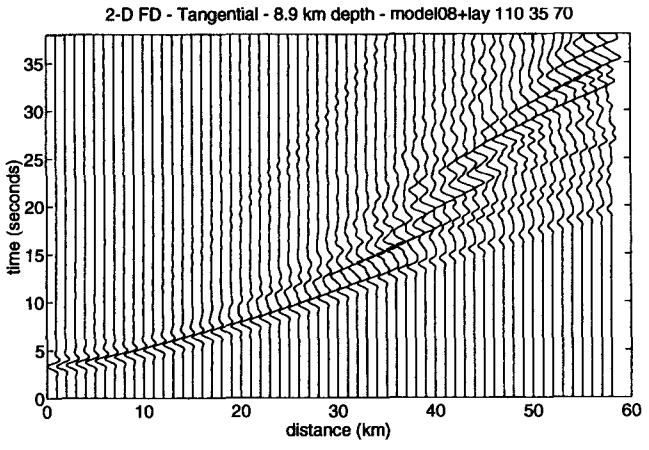

Figure 10. 2D finite-difference synthetic *SH* tangential displacement seismograms for a source at 8.9-km depth for the tomography model with a surface layer 0.5-km thick with a 50% reduction in velocity. Each trace is normalized by the peak amplitude.

km traversing the Santa Monica Mountains into the northern part of the basin. This is the key to increasing the amplitude and duration of energy in the coda and shows up even in simple modeling of dipping structures (Helmberger *et al.*, 1992; Helmberger and Vidale, 1988). The effect of the long-wavelength deeper-velocity structure is to provide energy arriving from a range of angles to interact with the near-surface layer. As discussed previously, imposing a lower-velocity layer above the tomographic model improves the fit of the waveforms significantly in dispersing the arrivals and extending the coda.

Complicated surface-wave coda observed in waveforms in the Los Angeles Basin has also been successfully modeled using a microbasin structure of low-velocity material, which traps and delays surface-wave energy (Saikia *et al.*, 1994; Graves, 1994). This has approximately the same effect on the waveforms as a possibly less realistic, thicker layer of low-velocity material. The low-velocity near-surface layer does not aid in modeling the very late coda. This extensive coda is most likely composed of energy arriving from off-azimuth directions. If there is an important 3D contribution, it most likely comes from multipathing of rays that intersect the basin edge not far from the radial direction, producing, in essence, a focusing due to concave structure (Olsen and Schuster, 1994). The narrowing of the northwest corner of the basin in the tomography model (Fig. 5) may produce just such an effect. A comparison between a 3D finite-difference calculation using this model and the 2D results would be an interesting way to investigate if the very smooth tomography model has enough curvature at the basin edge and sharp enough gradients to create these focusing effects.

The obvious next step is to improve the 3D tomography model of the Los Angeles Basin. This will involve the incorporation of well logs and other geological data to constrain the shallowest velocity structure. With information from more aftershocks, the timing and amplitude data from the waveform analysis can be incorporated into the tomographic inversion to further constrain the near-surface velocities. The surface-layer multiple phases are high enough amplitude to measure arrival times. Incorporation of all the portable arrival time data into the tomographic modeling to increase the resolution within the deepest part of the Los Angeles Basin and the extension of the tomographic modeling to include all of the San Fernando Valley will also be helpful in improving the tomographic model and the waveform fit. The focus of our research is evolving from verification of the 3D velocity model to developing methods of combining 3D tomography and waveform modeling to produce more complete synthetics of ground motions. The form of calibration of the tomography modeling described in this article is important for extending our ability to predict accurately strong ground motion anywhere within the Los Angeles Basin without waiting for a large damaging earthquake to occur.

Conclusions

We have used a two-dimensional slice of the 3D tomographic velocity model of the Los Angeles Basin to reproduce large-amplitude horizontal motions following the direct shear-wave arrival at stations within the basin. This is a feature that was observed in strong-motion recordings of the 17 January 1994 Northridge mainshock. The first-order effects of velocity variations seen in the data and synthetic record sections are the multiples reflected and trapped above the steep near-surface gradient. The increasing amplitude of the surface-layer multiples with distance in the recorded waveforms is caused by the dipping edge of the basin in the laterally varying velocity model. This traps and amplifies low-frequency energy. The sharpness of the gradient at the north end of the basin controls the timing of the *SS* arrival and whether or not it constructively interferes with the surface-layer multiples to produce large amplitudes.

Adding a thin low-velocity surface layer at the top of the tomographic model brings the timing of the secondary phases in the 2D finite-difference synthetics into close agreement with the arrivals observed in the data. The character of the waveforms at frequencies up to 1 Hz are very similar. This indicates that the 3D tomography model needs some refinement at the surface before it can be used for 3D finite-difference calculations. In particular, a modification to include lower velocities at the surface where the tomographic model has relatively poor resolution improves the fit at low frequencies and delays the phases so that they are more consistent with the data. The extensive coda more than 10 to 15 sec after the direct arrival observed for the basin stations cannot be modeled with this 2D structure. This indicates that three-dimensional propagation effects are important or that smaller wavelength features not resolvable by this method may play an important role in the very late coda.

Acknowledgments

We would like to thank the quick and effective team of the SCEC seismologists and technicians who deployed the instruments that provided the data for this work. We thank Dave Wald and Craig Scrivner who provided critical reviews that greatly improved this article. We would like to thank Don Helmberger and Doug Dreger for their helpful discussions. We would also like to thank Craig Scrivner and Xi Song for their help in using the programs to explore the range of possibilities for modeling the data. We thank Eric Calais for his help with the graphics. This work was supported by NSF Grant Number EAR 9416119 and the Southern California Earthquake Center. This is SCEC Contribution Number 181 and Caltech Division Publication 5510.

References

Alterman, Z. and F. C. Karal (1968). Propagation of elastic waves in layered media by finite difference methods, *Bull. Seism. Soc. Am.* **58,** 367–398.

Day, S. M., H. Magistrale, K. L. McLaughlin, and B. Shkoller (1994). Three-dimensional strong motion finite difference simulations of the Northridge Earthquake, *EOS* **75,** 168–168.

Dreger, D. S. and D. V. Helmberger (1990). Broadband modeling of local earthquakes, *Bull. Seism. Soc. Am.* **80,** 1162–1179.

Duke, C. M., J. A. Johnson, Y. Kharraz, K. W. Campbell, and N. A. Malpiede (1971). Subsurface site conditions and geology in the San Fernando earthquake area, UCLA-ENG-8206, School of Engineering, UCLA, Los Angeles, California.

Eberhart-Phillips, D. (1993). Local earthquake tomography: earthquake source regions, in *Seismic Tomography: Theory and Practice,* H. M. Iyer and K. Hirahara (Editors), 611–643.

Frankel, A. (1993). Three dimensional simulations of ground motions in the San Bernardino valley, California, for hypothetical earthquakes on the San Andreas fault, *Bull. Seism. Soc. Am.* **83,** 1020–1041.

Graves, R. W. (1994). Preliminary analysis of long-period basin response in the Los Angeles region from the 1994 Northridge Earthquake, *Geophys. Res. Lett.,* in press.

Hauksson, E. and J. S. Haase (1995). 3-Dimensional P-wave and S-wave Velocity Structure of the Los Angeles Basin, in preparation.

Hauksson, E. and J. Scott (1994). Refined 3-dimensional velocity structure of the L.A. basin, *Seism. Res. Lett.* **65,** 16.

Hauksson, E., L. M. Jones, and K. Hutton (1995). The 1994 Northridge earthquake sequence in California: seismological and tectonic aspects, *J. Geophys. Res.,* in press.

Heaton, T. H. (1982). The 1971 San Fernando earthquake: a double event?, *Bull. Seism. Soc. Am.* **72,** 2037–2062.

Helmberger, D., R. Stead, P. Ho-Liu, and D. Dreger (1992). Broadband modelling of regional seismograms: Imperial Valley to Pasadena, *Geophys. J. Int.* **110,** 42–54.

Helmberger, D. V. and J. E. Vidale (1988). Modeling strong motions produced by earthquakes with two-dimensional numerical codes, *Bull. Seism. Soc. Am.* **78,** 109–121.

Langston, C. A. (1978). The February 9, 1971 San Fernando earthquake: a study of source finiteness in teleseismic bodywaves, *Bull. Seism. Soc. Am.* **68,** 1–29.

Olsen, K. B. and G. T. Schuster (1994). Simulation of 3-D elastic propagation in the East Great Salt Lake (Weber) basin, *EOS* **75,** 441.

Olsen, K. B. and G. T. Schuster (1995). Causes of low-frequency ground motion amplification in the Salt Lake Basin—the case of the vertically incident P-wave, *Geophys. J. Int.* **122,** 1045–1061.

Saikia, C. K. (1994). Modified frequency-wavenumber algorithm for regional seismograms using Filon's quadrature: modelling of L_g waves in eastern North America, *Geophys. J. Int.* **118,** 142–158.

Saikia, C. K., D. S. Dreger, and D. V. Helmberger (1994). Modeling of energy amplification recorded within greater Los Angeles using irregular structure, *Bull. Seism. Soc. Am.* **84,** 47–61.

Scott, J. S., E. Hauksson, F. L. Vernon, and A. Edelman (1994). Los Angeles Basin structure from waveform modeling of aftershocks of the Jan. 17, 1994 Northridge earthquake, *Seism. Res. Lett., Northridge Supplement* **65,** 18.

Scrivner, C. W. and D. V. Helmberger (1994). Seismic waveform modeling in the Los Angeles Basin, *Bull. Seism. Soc. Am.* 1310–1326.

Shakal, A., M. Huang, R. Darragh, T. Cao, R. Sherburne, P. Malhotra, C. Cramer, R. Sydnor, V. Graizer, G. Maldonado, C. Petersen, and J. Wampole (1994). CSMIP strong motion records from the Northridge, California earthquake of 17 January 1994, *CSMIP Report No. OSMS 04-07.*

Steidl, J., A. Martin, A. Tumarkin, G. Lindley, C. Nicholson, R. Archuleta, F. Vernon, A. Edelman, M. Tolstoy, J. Chin, Y. Li, M. Robertson, L. Teng, J. Scott, D. Johnson, H. Magistrale, and USGS Staff (1994). Pasadena, Menlo Park, and Denver, SCEC portable deployment following the 1994 Northridge earthquake, *Seism. Res. Lett., Northridge Supplement* **65,** 1.

Thurber, C. (1993). Local earthquake tomography: velocities and Vp/Vs—theory, in *Seismic Tomography: Theory and Practice,* H. M. Iyer and K. Hirahara (Editors), pp. 611–643.

Tinsley, J. C. and T. E. Fumal (1985). Mapping quaternary sedimentary deposits for areal variations in shaking response, in *Evaluating Earthquake Hazards in the Los Angeles Region—An Earth-Science Perspective,* U.S.G.S. Professional Paper 1360, pp. 101–125.

Vidale, J. E. and D. V. Helmberger (1988). Elastic finite-difference modeling of the 1971 San Fernando, California earthquake, *Bull. Seism. Soc. Am.* **78,** 122–141.

Vidale, J., D. V. Helmberger, and R. W. Clayton (1985). Finite-difference seismograms for SH waves, *Bull. Seism. Soc. Am.* **75,** 1765–1782.

Wald, D. J. and T. H. Heaton (1994). A dislocation model of the 1994 Northridge, California, earthquake determined from strong ground motions, *USGS Open-File Report 94-278,* 53 pp.

Whitcomb, J. H., C. R. Allen, J. D. Garmany, and J. A. Hileman (1973). San Fernando earthquake series, 1971: focal mechanisms and tectonics, *Rev. Geophys. Space Phys.* **11,** 693–730.

Zhao, L. and D. V. Helmberger (1994). Source estimation from broadband regional seismograms, *Bull. Seismol. Soc. Am.* **84,** 91–104.

Seismological Laboratory 252-21
California Institute of Technology
Pasadena, CA 91125
(J.S.H., E.H.)

Institute of Geophysics and Planetary Physics
Scripps Institute of Oceanography
La Jolla, CA 92093
(F.L.V., A.E.)

Manuscript received 9 January 1995.